Article

Novel 3D Printed Biocarriers from Aluminosilicate Materials

Eleni Anna Economou [1], Savvas Koltsakidis [2], Ioanna Dalla [1], Vesna Middelkoop [5], Konstantinos Tsongas [2,3], George Romanos [4], Dimitrios Tzetzis [2], Polycarpos Falaras [4], George Theodorakopoulos[4] and Themistoklis Sfetsas [1,*]

[1] QLAB Private Company, Research & Development, Quality Control and Testing Services, 57008 Thessaloniki, Greece; t.sfetsas@q-lab.gr
[2] Digital Manufacturing and Materials Characterization Laboratory, School of Science and Technology, International Hellenic University, 57001, Thessaloniki, Greece
[3] Department of Industrial Engineering and Management, School of Engineering, International Hellenic University, 57001 Thessaloniki, Greece
[4] Institute of Nanoscience and Nanotechnology, National Center of Scientific Research "Demokritos", Agia Paraskevi, Athens, 15310, Greece, g.romanos@inn.demokritos.gr, g.theodorakopoulos@inn.demokritos.gr
[5] Sustainable Materials Management, Flemish Institute for Technological Research, VITO, Boeretang 200, 2400 Mol, Belgium
* Correspondence: t.sfetsas@q-lab.gr; Tel.: +30 2310 784712

Abstract: The addition of biocarriers can improve the biological processes appearing in a bioreactor since their surface allows the immobilization, attachment, protection, and growth of microorganisms. In addition, the development of a biofilm layer allows the colonization of microorganisms in the biocarriers. The structure, composition, and roughness of the biocarriers' surface are crucial factors that affect the development of the biofilm. In the current work, the aluminosilicate zeolites 13X and ZSM-5 were examined as the main building components of the biocarrier scaffolds, using bentonite, montmorillonite, and halloysite nanotubes as inorganic binders in various combinations. 3D printing was utilized to form pastes into monoliths that underwent heat treatment. The 3d-printed biocarriers were subjected to a mechanical analysis, including density, compression, and nanoindentation tests. Furthermore, the 3d-printed biocarriers were morphologically and structurally characterized using nitrogen adsorption at 77 K (LN_2), scanning electron microscopy (SEM), and X-ray diffraction (XRD). The stress-strain response of the materials being studied was obtained through nanoindentation tests combined with finite element analysis (FEA). These tests were also utilized to simulate the lattice geometries under compression loading conditions to investigate their deformation and stress distribution in relation to experimental compression testing. The results indicated that the 3d-printed biocarrier 13X/halloysite nanotubes was endowed with high specific surface area and extended mesoporous structure. Due to these assets, its bulk density was one of the lowest observed amongst the biocarriers derived from the various combinations of materials. The biocarriers based on the 13X zeolite exhibited the highest mechanical stability and appropriate morphological features. The 13X/halloysite nanotubes scaffold exhibits a moderate hardness value compared to the rest, while it presents the highest value of modulus of elasticity. In conclusion, Aluminosilicate zeolites and their combination with clays and inorganic nanotubes afford 3d-printed biocarriers of various textural and structural properties, which can be utilized to improve biological processes.

Keywords: aluminosilicate clays; zeolites; biocarriers; inorganic nanotubes; 3D printing

1. Introduction

Zeolites are highly porous crystalline aluminosilicates formed by SiO_4 and AlO_4 tetrahedra. These materials have a wide range of applications as sorbents, ion exchangers in detergents, catalysts in the oil refining and petrochemical industry, and in waste treatment processes [1,2].

 doi:10.20944/preprints202305.1849.v1

In bioreactors, during waste treatment, a variety of byproducts might be produced depending on the digestion type performed. The application of biocarriers is one method for increasing productivity in bioreactors. Biocarriers frequently consist of porous surfaces where bacteria can adhere to create biofilms. They can be manufactured from reactive organic materials (alginate), inert materials (polyvinyl alcohol, or PVA), or inorganic materials (zeolite). Due to the increased surface area, biocarriers increase the productivity of the bioreactor and shield the attached microorganisms from the forces of the bioreactor [27].

Various methods are available for the synthesis of zeolite monolithic structures such as extrusion [3], inverse replication [4,5], dry gel conversion [6], 3D printing [7,8,9,10], wash coating [11], hydrothermal coating [12] or a combination of the last two [13]. However, not all can be applied for the synthesis of bulk zeolite structures, as the final material needs to have high porosity for the accessibility of the pores and active sites. Some methods of zeolite 3d printing, such as Direct Ink Writing (DIW), are similar to the less sophisticated method of extrusion, which has already been widely investigated [3,14]. However, the impact of different binders for manufacturing zeolite monoliths through 3d printing for wastewater treatment is not yet fully understood.

3D printing applications for manufacturing the functional components of chemical, biochemical and environmental processes have been significantly increased in the last several years [15]. 3D printing technologies have an advantage over conventional production techniques by allowing for bespoke design of the biocarrier, achieving customized shape, microstructure, and multi-material compositions for homogeneous dispersion of the active species, as well as efficient diffusion and mass transfer. In addition, the application of 3D printing technology has various benefits, including less waste produced during geometry machining and reduced material consumption for geometry fabrication [16,17]. The variety of materials utilized to create the ceramic biocarriers has a significant impact on both the porosity and mechanical strength of the printed structure. Some recent studies have highlighted the effect of binder in the psychochemical properties of zeolite monoliths. Researchers in [18] created monoliths using ZSM5 and examined how the concentration of bentonite clay binder impacts the rheological, physicochemical, and mechanical characteristics. Their findings revealed that higher concentration of binder leads to a more uniform material with enhanced mechanical strength but deteriorates the physicochemical properties. In another study [19] researchers found that the final sample's porosity is decreased by the frequent use of inorganic binders at high concentrations. In reference [20], research investigations demonstrated that the choice of binder in the formulation of 3D printed structures significantly influences the printing process, the calcination stage, and the physicochemical properties of the resulting structure.

In this work two zeolites were selected as the basic structural components. The selection was made primarily due to their different Si/Al ratios, which ranged from extremely low (13X) to high (ZSM-5), but also due to the variation of their pore structural features (pore size and shape, tortuosity, porosity) and the large difference of their particle size (0.5 μm for ZSM-5 and 5 μm for 13X). The inorganic binders utilized are inorganic halloysite nanotubes, montmorillonite, and bentonite. The different Si/Al ratios of the chosen zeolites combined with the silicon-rich structure and the different size, shape and expanding capacity of the above-mentioned phyllosilicate binders allow for massive experimentation to determine which zeolite/binder combinations, and in what mass ratio, are suitable for developing biocarriers with enhanced resistance to attrition and erosion and improved structural and morphological features that augment the bioprocess performance [21]. 3D printing technology is used to develop carrier aluminosilicate scaffolds to efficiently immobilize enzymes for tailored continuous flow biocatalytic reactors. The resulting 3d-printed biocarriers underwent mechanical testing to evaluate their density, compression, and nanoindentation. Additionally, the biocarriers were analyzed using techniques such as nitrogen adsorption at 77 K (LN2), scanning electron microscopy (SEM), and X-ray diffraction (XRD) to examine their structural and morphological characteristics.

Preprints (www.preprints.org) | NOT PEER-REVIEWED | Posted: 26 May 2023 doi:10.20944/preprints202305.1849.v1

2. Materials and Methods

Ceramic material ZSM-5 (Thermo Fisher Scientific Inc., Waltham, MA, USA) or 13X zeolite (Alfa Aesar, Ward Hill, MA, USA) was combined with inorganic phyllomorphous porous solids (montmorillonite or bentonite, or halloysite nanotubes) and an organic binder to create the printing paste. Following that, a colloidal silicon/ionized aqueous solution was created. For effective production of printed ceramic paste, the paste's solid content must be more than 50% in order to obtain maximum density and avoid excessive shrinkage during drying and calcination. Finally, the colloidal silicon/ionized water mixture was gradually blended with the solid mixture. The final mixture was mechanically agitated until it took on the consistency of a viscous paste. To decrease agglomeration that occurred during preparation, the paste was transferred to an iron plate and handled with a metal spatula. For the complete subtraction of aggregates, a sieve with a diameter of 45 μm was utilized. A metal spatula was used to push the paste through the pores of the sieve. The pore diameter of the final agglomerate-free paste was less than 45 μm.

Cellink's Bio X6 (Gothenburg, Sweden) printer, which is based on Direct Ink Writing (DIW), was utilized to print the biocarriers. Following the manufacturing process, the paste was carefully inserted into the syringe to avoid the formation of air bubbles. The material was then centrifuged to eliminate any remaining air bubbles. The syringe was then inserted into the printer, where print preparation occurred. The 3D geometry was created, and parameters such as the shape of the biocarriers, the recurring geometric pattern, the height of each layer, the nozzle diameter, the pressure, and the printing speed were set. The chosen geometric pattern can be defined as rectilinear. Each layer was printed in a single direction, with the next layer printed perpendicular to the previous one (90°). Its dimensions were 24 mm wide, 14 mm length, and 7 mm height. The density of the repeating geometric pattern was 18% **(Figure 1**).

For high-resolution printing attachments, the particles must be minor than the diameter of the nozzle used to print the paste, ensuring that the mixture is homogenous and free of agglomerations. The zeolite and alumina silicate binders were made in various quantities, with solids contents ranging from 44% to 61%. Due to the clarity level being kept low, the final structure was primarily zeolite while retaining good mechanical strength. The ratio of colloidal silicon to clay was likewise kept constant at 2.5. The zeolite and argil mixing ratio in the paste was 8:1, with relative amounts of 89% and 11%, respectively. The Bio X6 printer is capable of printing a volume of 128 x 90 x 90 mm (W x L x H) with an accuracy of 1 μm (arm movement). Furthermore, the printer allows print heads to be heated from 4 °C to 250 °C, allowing the viscosity of ceramic pastes to be adjusted, while the print surface can be cooled to 4 °C for better-printed structures.

Figure 1. Novel 3D-printed zeolite biocarriers.

The Autosorb-1-MP adsorption analyzer of Quantachrome was used to obtain the N_2 adsorption-desorption isotherms (77 K) and extract the pore structural properties including the BET surface, the micropore and mesopore volume and the pore size distributions. For the latter, the Non-Local Density Functional Theory (NLDFT) method for silica and N_2 as adsorbate was applied to interpret both the adsorption (adsorption model-cylindrical pores) and desorption (equilibrium model-cylindrical pores) branches of the isotherm. Before the measurement, all samples were outgassed at high temperature (300 °C) and high vacuum conditions (10-5 mbar) for 24 hours.

A Jeol JSM-7401F Field Emission Scanning Electron Microscope equipped with Gentle Beam mode was employed to characterize the surface morphology of the biocarriers. Gentle Beam

Preprints (www.preprints.org) | NOT PEER-REVIEWED | Posted: 26 May 2023 doi:10.20944/preprints202305.1849.v1

technology can reduce charging and improve resolution, signal-to-noise and beam brightness. Scanning electron microscopy (SEM) was performed at typical conditions of 10 mA of emission current and 2 kV of operating voltage.

The XRD diffraction patterns were recorded on a Rigaku R-AXIS IV Imaging Plate Detector mounted on a Rigaku RU-H3R Rotating Anode X-ray Generator (operating at 50 kV, 100 mA, nickel-filtered Cu Ka1 radiation). The samples were sealed in Lindemann capillaries. The X-ray diffraction (X-RD) technique is used to study parameters of material crystallinity. Electrons that hit the target gradually lose their energy as they are slowed down by the atoms of the metallic material. Through the collision, the electrons impart energy to the atoms of the target, such that it causes the electrons of the inner shells of the atoms to be excited as well. Thus, characteristic X-rays are produced as these layers are filled with higher energy electrons.

To determine the compressive strength of the biocarriers that were printed and thermally treated, uniaxial tests were conducted on the samples. The tests were carried out at room temperature using a universal testing machine (M550-50AT, Testometric, UK) with a crosshead that moved at a constant rate of 1mm/min. The loads applied during the tests were recorded using a loadcell with a resolution of 1mN. To calculate stress, the compressive force was divided by the measured cross-sectional area of each sample. A minimum of 3 samples were tested for each composition, and the compressive strength was determined by identifying the maximum stress reached on the force-displacement curves obtained from the tests.

To improve the accuracy of the compression tests for the biocarriers, a finite element model (FEM) has been developed [22]. The ANSYS™ software was used to investigate the mechanical behavior of various structures. The explicit dynamic module was employed to accurately simulate the response of lattices with dynamic finite element analyses. This process helped to capture their deformations, non-linear material behavior and different fracture modes. A model that combines damage mechanics and plasticity has been developed to analyze the failure of ceramic structures. The objective is to create a model that accurately describes the key aspects of the failure process when ceramics are subjected to uniaxial loading. To achieve this, an effective stress-based plasticity model is combined with a damage model that considers plastic and elastic strain measures. The model's response under compression was compared to experimental data. To obtain mesh-independent results, mesh sensitivity analyses were conducted using convergence studies on normalized elastic modulus, as per the literature. The studies revealed that convergence was achieved with nearly 100,000 elements for each model. Hexahedral elements were utilized with a size of 0.1 to 0.5 mm (average 0.3 mm) to fit the complex geometry of lattice structures.

The nanoindentation measurements were carried out on a DUH-211S Shimadzu (Kyoto, Japan) device with a diamond triangular tip Berkovich indenter (angle of 65°, tip radius is 100nm) and a force resolution of 0.196μN. The modulus and hardness were determined based on the work of Oliver and Pharr [23,24,25]. The maximum load observed was 100 mN and it was achieved with a rate of 6.662 mN/sec.

3. Results

3.1. Pore structural and textural features of the Novel 3D-Printed Biocarriers

Nitrogen adsorption (77 K) isotherms were obtained not only for the shaped biocarriers but also for all the inorganic materials involved in their development. Apart from ellaborating the pore structural and textural features of the biocarriers' basic components, the main target of this approach was to achieve prediction of the nitrogen adsorption isotherms of the end products, being aware of the mass ratio of their basic components (zeolites/inorganic binders, 8:1) and assuming that the final structure entails solely a physical mixing process of the two powders. Explanatively, the adsorption isotherm is predicted with the assumption that the use of inorganic and organic binders along with the further calcination of the raw biocarriers do not affect the pore structural characteristics of the parent zeolites. Thence, we admitt that the N_2 adsorption isotherm of the calcined structure coincides with the one corresponding to a sample produced by physically mixing the two powders (zeolite and

 doi:10.20944/preprints202305.1849.v1

inorganic binder) at a specific mass ratio. Despite, significant deviations are expected between the predicted isotherm and that of the real sample. Negative deviation can be related to the loss of a fraction of the pore volume due to sintering or due to carbon remnants of the organic binder after calcination (blockage of the pore entrance). It is also possible that part of the meso-macropore structure of the parent zeolite is lost due to coverage by the binder particles in a core-shell structure. The more interesting cases however are those where synergistic effects arising due to the size, shape, surface chemistry, expanding capacity and nesting conformation of the inorganic binder particles, conclude to positive deviations of the real adsorption isotherm compared to the predicted one. As such, the interpretation of the N_2 adsorption isotherms (77 K) of the real samples led to the pore structural properties presented in Table 1, while a comparison of the real and predicted isotherms of the shaped biocarriers is depicted in Figure 1a-f.

The results included in Table 1 indicate that 13X zeolite is an almost purely microporous material with a narrow pore size distribution centered around 10 Å. As such, 13X exhibited larger specific surface area, micropore volume, and micro- and mesopore size than ZSM-5 zeolite. ZSM-5 zeolite, on the other hand, has more complex characteristics, possesing an hierarchical pore structure with distinctive bimodal pore size distribution and higher total pore volume and mesopore volume than 13X zeolite (**Table 1**).

The various zeolite/inorganic binder combinations result in the development of complex materials with novel properties and applications. The 13X/Montmorillonite had a greater total pore volume and a bigger volume of mesopores than the pure 13X zeolite, but it also had a smaller specific surface area, as well as a smaller volume and diameter of micropores. 13X/Bentonite had larger total pores and mesopores volume than 13X but showed a decrease in specific surface area, micropore volume, and diameter.

Although the 13X zeolite had a high specific surface area, its combination with the inorganic binders reduced it, with the exception of 13X/Halloysite nanotubes, which showed an increase in specific surface area, total volume of pores, and mesopore volume. However,the diameter of the micropores was smaller. The ZSM-5/Bentonite mixture exhibited similar behavior, with a larger diameter value than pure ZSM-5.

The general characteristics of the composites containing 13X and ZSM-5 zeolites decreased as expected due to lower specific surface area and micro- and mesopore volume of the inorganic binders. The best complex zeolites, according to BET analysis, were 13X/Halloysite nanotubes and ZSM-5/Bentonite. The same conclusion is drawn by examining the comparison plots of the real and predicted N_2 adsorption isotherms (77 K) of the 3D printed biocarriers (**Figure 1a-f**). It can be seen that in all cases where the 13X zeolite was used as the core material of the biocarrier (**Figure 1a-c**), the real isotherm of the 3d-printed scaffold unveils higher mesopore volume than the predicted one. In some cases, this trend is monotonic covering the entire range of pore sizes, from the micropores to the macropores. Solely in the 13X/Bentonite sample the real micropore volume is lower than the one derived from the predicted isotherm and this may be connected with the expanding capacity of bentonite compared to the other two binders. In general there is an impressive synergistic effect achieved by the mixing/3d-printing and calcination of the 13X zeolite with all the inorganic binders that leads to enhanced mesoporosity, a feature that was missing from the parent 13X zeolite material. In fact the mesopore volume of the obtained biocarriers is larger than that of each individual component. On the contrary, in all cases that ZSM-5 was involved as the core material for the deployment of the biocarriers, the real isotherms show moderate pore structural features as compared to the ones derived from the predicted isotherm (**Figure 1e-f**). This different trend can be attributed to the variation in the morphology and size of the crystallites of the two zeolites and to their highly different surface acidity (Si:Al ratio) that may lead to better dispersion of the binder's particles around the particles of the zeolitic material (13X), thus concluding to a more effective sintering process during the calcination of the raw biocarrier. Another cause can be related with the different pore structure of the two zeolites. ZSM-5 is characterised by smaller micropores and a quite extented mesopre structure as compared to 13X. As such, the mixing with the inorganic binder seems to have an adverse effect on the mesopore structure of the ZSM-5 zeolite. This is also proclaimed by

Preprints (www.preprints.org) | NOT PEER-REVIEWED | Posted: 26 May 2023 doi:10.20944/preprints202305.1849.v1

the results presented in Table 1 showing that the shaped biocarrier scaffold exhibits lower mesopore volume compared to the pristine ZSM-5 material.

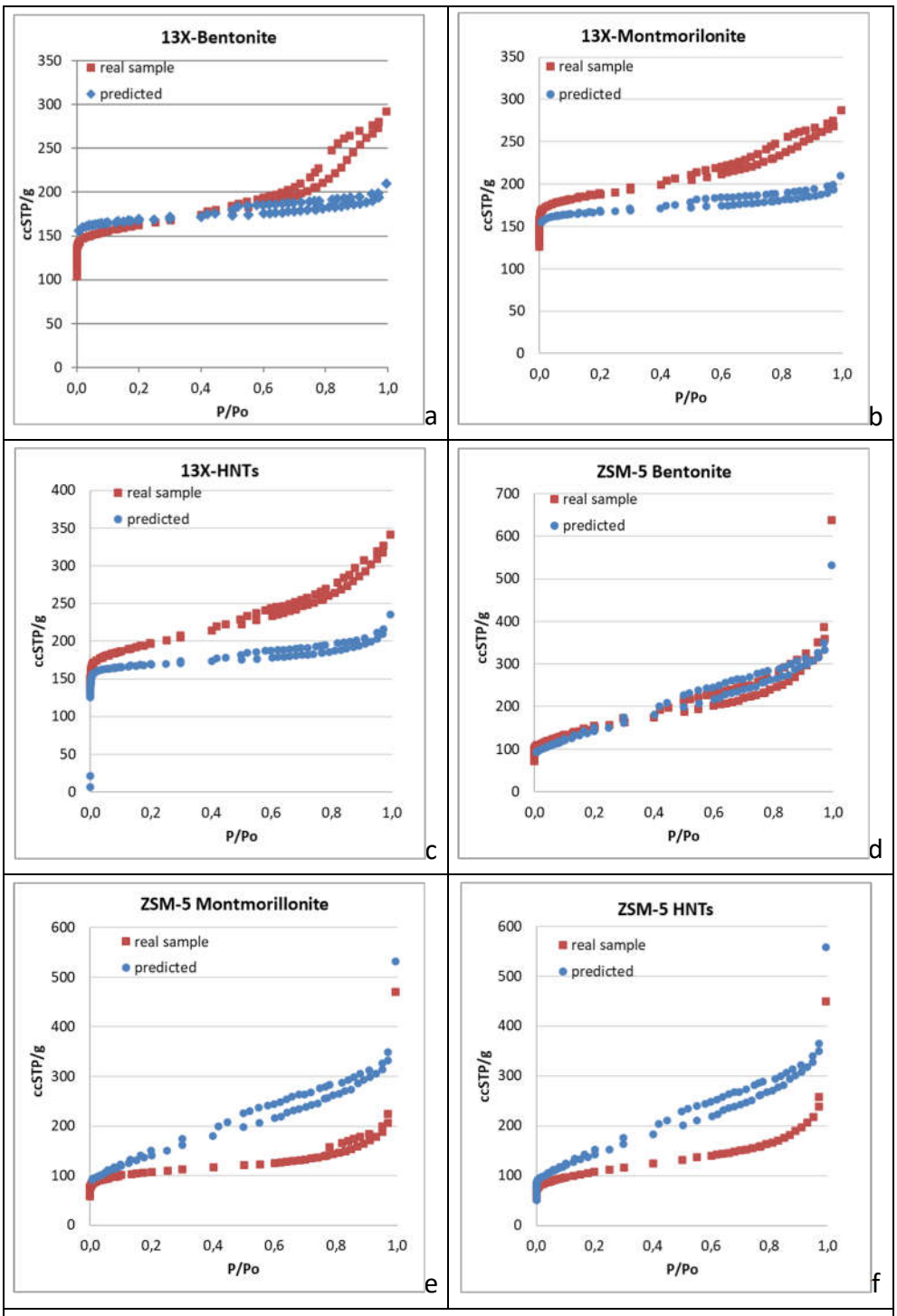

Figure 1: Comparison between the real and predicted N2 adsorption-desorption isotherms (77K) of the examined in this work biocarriers. (a-c) 13X with bentonite, montmorillonite and HNTs. (e-f) ZSM-5 with bentonite, montmorillonite and HNTs.

Preprints (www.preprints.org) | NOT PEER-REVIEWED | Posted: 26 May 2023 doi:10.20944/preprints202305.1849.v1

Table 1. Surface area, pore volume, and size of innovative 3D-printed biocarriers compared to original materials.

	Specific Surface Area (m^2/g)	Total Pore Volume (cc/g)	Micropore Volume (cc/g)	Mesopore Volume (cc/g)	Micropore Diameter (Angstrom)	Mesopore Diameter (Angstrom)
13X	688	0,35	0,29	0,06	10,2	55
ZSM5	549	0,57	0,21	0,36	5	42
Bentonite	52	0,15	0,02	0,13	na	55
Montmorillonite	32	0,16	0,01	0,15	na	55
Halloysite Nanotubes	89	0,32	0,03	0,29	na	55 and 116
13X/Bentonite	590	0,42	0,24	0,18	9	42, 116
13X/Halloysite Nanotubes	711	0,49	0,29	0,20	9	34, 55, 97
13X/Montmorillonite	687	0,42	0,28	0,14	9	39, 54, 94
ZSM5/Bentonite	527	0,56	0,21	0,35	9,4	35, 51, 116
ZSM5/ Montmorillonite	397	0,32	0.16	0.16	9	24, 35, 54
ZSM5/Halloysite Nanotubes	383	0,37	0,15	0,22	9	35, 53, 78

3.2. Density Analysis of 3D-Printed Biocarriers

The addition of a different inorganic binder (clay) to 13-X causes differences in the density of the final material presented in **Table 2**. The lowest density appears in the mixture of 13X and bentonite. It should be underlined that the material's low density is desirable in order for the biocarriers to be more easily suspended under agitation conditions (aeration or stirring). The addition of different clays to ZSM-5 zeolite did not cause a significant difference in the densities of the biocarriers. In contrast, zeolite ZSM-5 produces materials with the highest density of 1.97 g/ml of any zeolite/clay combination.

Table 2. Density measurements of 3D-printed biocarriers.

3D-Printed Biocarriers	Density of Biocarriers (g/cm^3)
13X/Bentonite	1,42 ± 0,03
13X/Montmorillonite	1,64 ± 0,03
13X/Halloysite Nanotubes	1,67 ± 0,02
ZSM5/Bentonite	1,97 ± 0,01
ZSM5/Montmorillonite	1,98 ± 0,16
ZSM5/Halloysite Nanotubes	1,94 ± 0,20

3.3. Mechanical Properties Analysis

The results obtained from the nanoindentation test data are plotted in **Figure 2**. The graph shows the relationship between the applied force and the resulting displacement during the indentation test. During the loading curve, a probe is pushed into the surface of the material with a continuously increasing force, while the displacement of the probe is recorded so it is possible to calculate the material's hardness. Once the maximum force is reached, the probe is then retracted from the material, and the unloading curve is recorded. The unloading curve shows the relationship between the applied force and the displacement as the probe is withdrawn from the material and from the slope one can calculate the material's modulus of elasticity. The results lead to the conclusion that both the hardness and the modulus of elasticity of the biocarriers made of 13X are higher than those

Preprints (www.preprints.org) | NOT PEER-REVIEWED | Posted: 26 May 2023 doi:10.20944/preprints202305.1849.v1

of the biocarriers made of ZSM-5. Regarding the effect of the binder on the modulus of elasticity and hardness there is no clear trend.

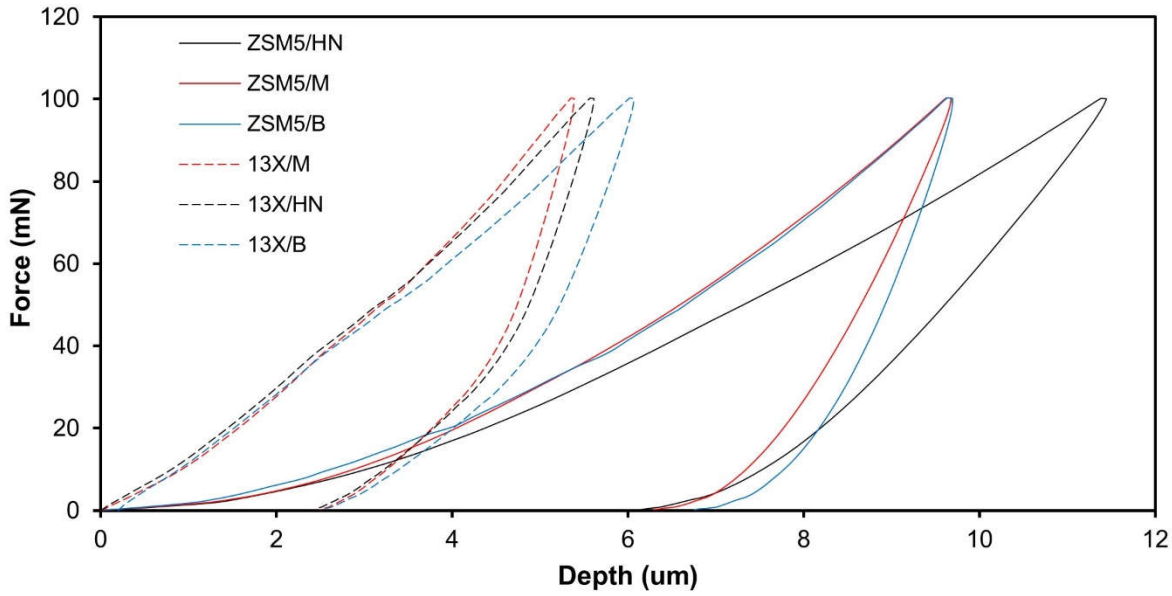

Figure 2: Nanoindentation results combining different zeolites and binders.

It should also be noted that the hardness and modulus of elasticity are of the same order of magnitude, apart from the modulus of elasticity of the ZSM-5/Halloysite Nanotubes combination, which is an order of magnitude lower than the rest (**Table 3**). The greater hardness was achieved with the 13X/Montmorillonite combination with a value of 52.57 MPa. The results obtained from the nanoindentation tests were utilized as input to conduct a finite element (FE) analysis on the mechanical behavior of the biocarriers.

Table 3. Hardness and Elastic modulus values obtained through nanoindentation.

3D-Printed Biocarriers	Hardness (MPa)	Elastic Modulus (MPa)
13X/Bentonite	44.35 ± 5.39	3378.67 ± 383.89
13X/Halloysite Nanotubes	45.64 ± 5.47	3422 ± 130.11
13X/Montmorillonite	52.57 ± 4.60	3223 ± 335.71
ZSM5/Bentonite	38.45 ± 7.64	1347.75 ± 47.53
ZSM5/Montmorillonite	38.21 ± 2.37	1188.5 ± 204.19
ZSM5/Halloysite Nanotubes	29.01 ± 6.01	545.5 ± 52.39

Compression tests were carried out on samples and representative stress – strain curves are presented in **Figure 3**. All specimens presented a multipeak profile due to successive noncritical failures. The repetition of this behavior produces a jagged stress–strain curve until a relatively sharp decrease in stress which indicates the critical failure. The results of the compression tests lead to the conclusion that the biocarriers made of 13X present a higher resistance to compression (**Table 4**). The effect of inorganic binders does not follow any common trend in any biocarriers. The highest compressive strength is shown by the combination of 13X and montmorillonite with a value of 261 KPa. Furthermore, to assess the stress response of the 3D-printed specimens under compression, a computational model was utilized. This model was developed through the ANSYS™ finite element software and incorporated initial stress-strain values obtained from nanoindentation tests of the 3D

Preprints (www.preprints.org) | NOT PEER-REVIEWED | Posted: 26 May 2023 doi:10.20944/preprints202305.1849.v1

materials. A vertical velocity was applied in increments to the top plate of each lattice structure, and the resulting reaction force at the bottom was obtained, taking into account a fixed boundary condition. The vertical displacement values were obtained from the experimental results. Deformation was taken into consideration and the resulting forces were compared to the experimental results. A hexahedral mesh was used for both the top compression plate and the 3D printed biocarriers. **Figure 3c** presents the stress-strain behavior obtained from the finite element analysis (FEA) results, which showed a strong correlation between the experimental compression tests and the force-displacement data generated by the FEA simulations for the 3D-printed specimens. However, it is important to note that at larger displacements, the experimental curves begin to diverge more from the FEA simulation because the 3D printing defects have a greater impact on the bending response. The material model parameters were analyzed to minimize the difference between the simulated and experimental stress-strain data. As a result, the deformation and the equivalent stress distribution of the 3D-printed lattice structures under compressive load, as presented in **Figure 3d, e**, could precisely identify the high-stress regions of the structures. Based on the mechanical test results, it can be concluded that the computationally generated (FEA) compression test data, with the assistance of actual measurements, could be a reliable approach to evaluate the mechanical deformation behavior of 3D-printed lattice biocarriers.

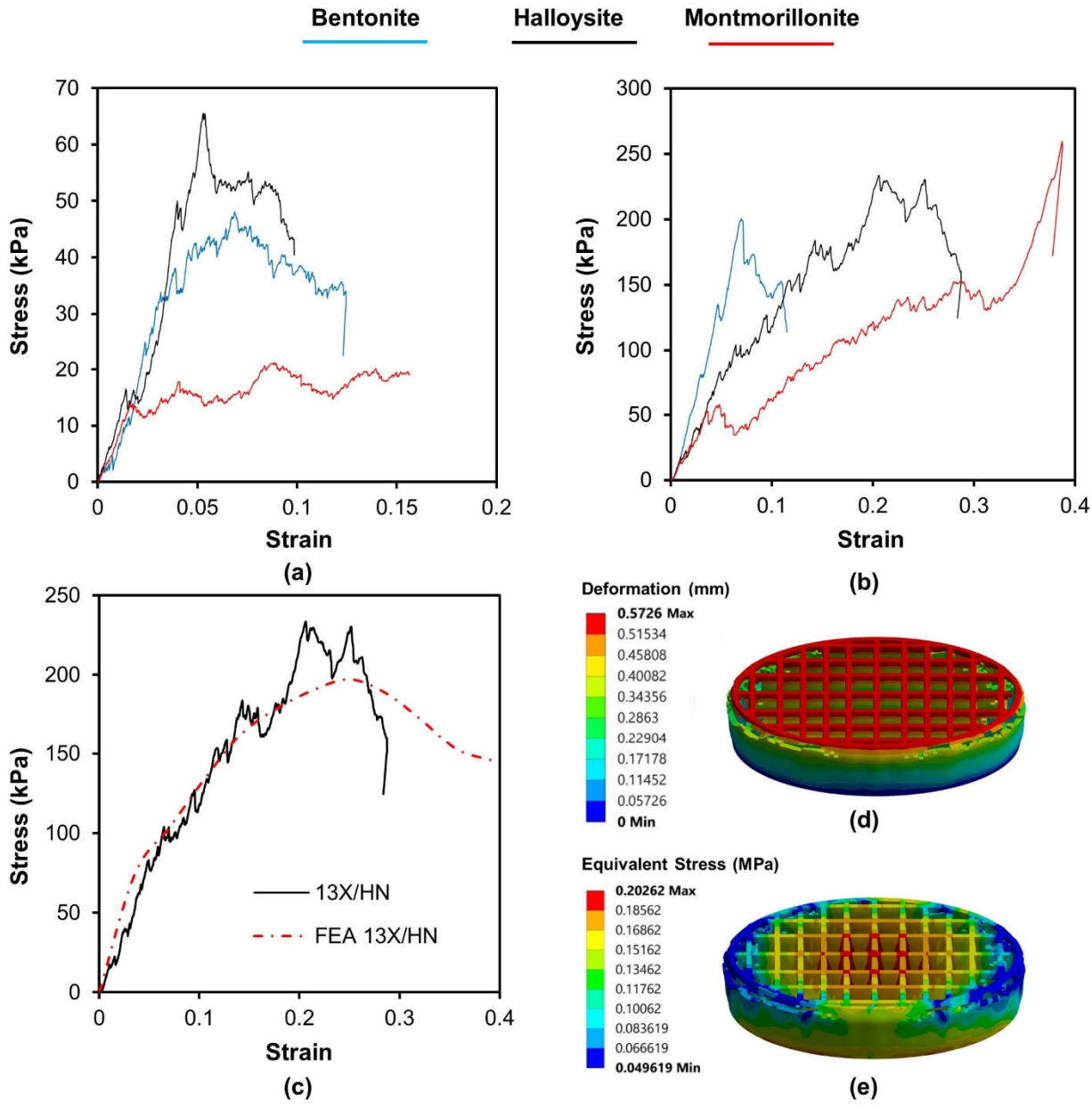

Preprints (www.preprints.org) | NOT PEER-REVIEWED | Posted: 26 May 2023 doi:10.20944/preprints202305.1849.v1

Figure 3: Compression results for (a) ZSM5 zeolite combined with different binders and (b) 13X zeolite combined with different binders and (c) FEA generated compression test results compared to experimental values of 13X specimens along with (d) vertical deformation and (e) stress distribution of the structure under compression load, utilizing the 13X/HN material properties in the FE model.

Table 4. Compression test results.

3D-Printed Biocarriers	Compressive strength (kPa)
13X/Bentonite	175.85 ± 34.93
13X/Halloysite Nanotubes	215.89 ± 35.36
13X/Montmorillonite	261 ± 2.28
ZSM5/Bentonite	50.95 ± 10.38
ZSM5/Montmorillonite	20.52 ± 4.90
ZSM5/Halloysite Nanotubes	57.78 ± 11.05

3.4. Scanning Electron Microscopy (SEM) Analysis of the Novel 3D-Printed Biocarriers

Figures 4a and 5a show a significant differece in the particle size of the pristine zeolitic materials. In specific 13X exhibits a particle size of about 5 μm and this possibly explains the synergistic effects achieved in the pore structural features of the 3d printed scafolds as discussed in section 3.1. In specific the large particle size allows for the existence of more space between the 13X particles. As a result, the particles of the clay binders are better dispersed between the particles of the 13X zeolite and this concludes to higher mechanical stability of the respective biocarriers as well as to the creation of extented mesoporosity. In general, according to SEM images of the 13X biocarriers, a high degree of dispersion is observed in all three combinations, with the 13X/Halloysite Nanotubes biocarrier (**Figure 4b**) exhibiting better behavior. This property of the material is due to the combination of the high specific surface area of the 13X zeolite with the ability of the halloysite nanotubes, due to their elongated shape, to better disperse and nest in the void space between the zeolite particles. Similar behavior is also observed in the ZSM-5 zeolite-based biocarriers, with the ZSM5/Bentonite biocarrier (**Figure 5a**) showing the best dispersion.

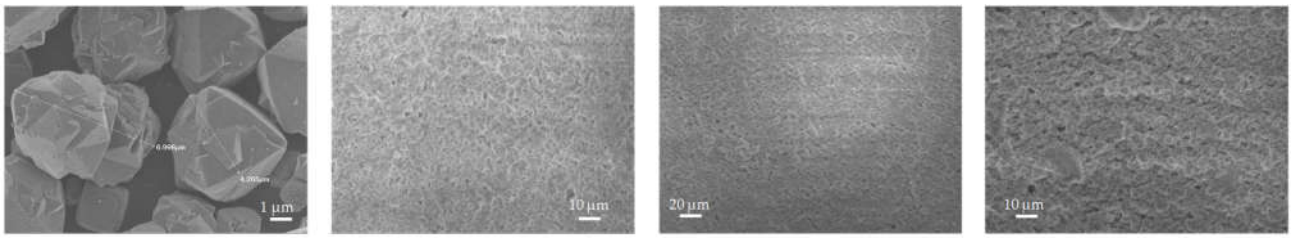

(a) (b) (c) (d)

Figure 4: SEM images of **a)** pristine 13X particles, **b)** 13X/Bentonite, **c)** 13X/Halloysite Nanotubes, and **d)** 13X/Montmorillonite 3D-printed biocarriers.

Preprints (www.preprints.org) | NOT PEER-REVIEWED | Posted: 26 May 2023 doi:10.20944/preprints202305.1849.v1

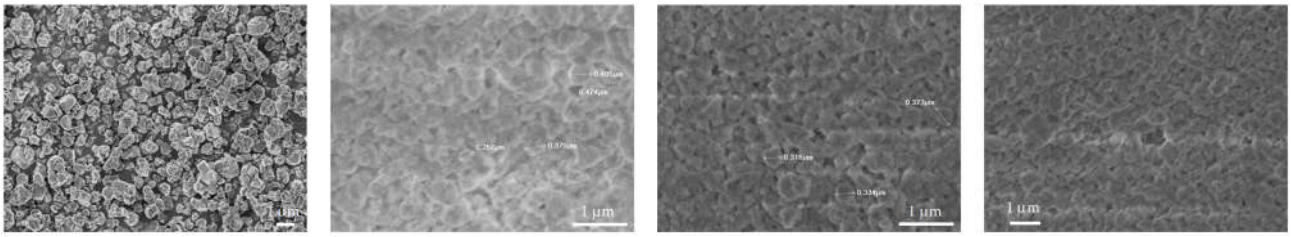

(a) (b) (c) (d)

Figure 5: SEM images of **a)** pristine ZSM-5 particles, **b)** ZSM5/Bentonite, **c)** ZSM5/Halloysite Nanotubes, and **d)** ZSM5/Montmorillonite 3D-printed biocarriers.

3.5. X-Ray Diffraction (X-RD) Analysis of the Novel 3D-Printed Biocarriers

The X-RD spectra of zeolite 13X with all three combinations of inorganic materials (bentonite, halloysite nanotubes, and montmorillonite) show the characteristic peaks of zeolite 13X, which overlap the peaks of the inorganic binders (**Figure 6**). This fact is due to the large amount of zeolite 13X in relation to the corresponding inorganic materials, as the percentage of bentonite, halloysite nanotubes, and montmorillonite respectively in the final biocarrier corresponds to 11%. This percentage is calculated from the quantities of raw materials used to prepare the mixture.

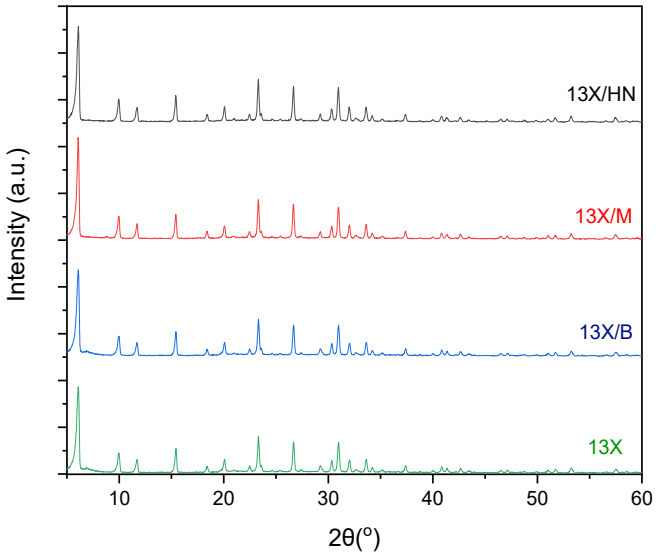

Figure 6: X-RD spectra of 13X-based zeolites 3D-printed biocarriers.

This occurrence is also observed in the X-RD spectra of the ZSM-5 zeolite with bentonite, halloysite, and montmorillonite nanotubes, which is due to the final biocarrier's equally low percentage of inorganic binders (11%) (**Figure 7**). Furthermore, in the spectra of ZSM5/Bentonite, ZSM5/Halloysite Nanotubes, and ZSM5/Montmorillonite, a peak drop between 22.5° and 25° was observed. The appearance of disturbances during the incorporation of clays into the ZSM-5 zeolite can be attributed to the variation in the peaks [26].

Preprints (www.preprints.org) | NOT PEER-REVIEWED | Posted: 26 May 2023 doi:10.20944/preprints202305.1849.v1

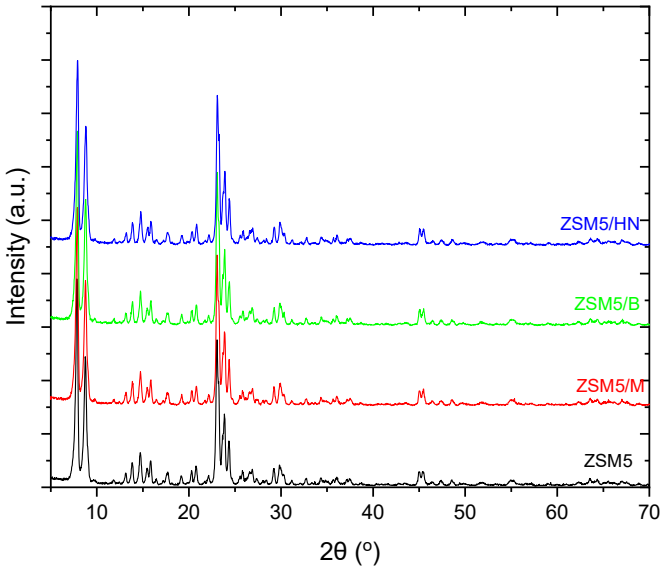

Figure 7: X-RD spectra of ZSM-5 based zeolites 3D-printed biocarriers.

5. Conclusions

In this work, different aluminosilicate binders were used in order to produce zeolite monoliths through 3d printing. The various zeolite–binder combinations have led to complex materials with improved properties and consequently increased applications' performance.

The result indicated that, even though 13X zeolite has a high specific surface area, it is reduced when combined with other zeolites. This can be attributed to smaller molecules of 13X zeolite which results in reduced. The main reason for this phenomenon is that the molecules of the 13X zeolite are smaller than those of the others, reducing the degree of dispersion. Despite having the highest specific surface area, the 13X/Halloysite Nanotubes composite has larger specific surface area, total pore volume, and micro- and mesopore volume. It is well known that nanotubes can allow molecules to disperse inside them, enhancing the dispersion degree of the 13X zeolite. Furthermore, because of the ability to distribute synthetic substances, other complex materials containing 13X zeolite have lower values of specific surface area and pore volume. Despite the fact that nanotube materials can increase the degree of dispersion of materials' molecules, ZSM5/Halloysite Nanotubes diminish the specific surface area as well as other parameters. This reduction in surface area may be due to the clogging of some pores by the permanent binder and the large number of total pore and mesopore volumes of ZSM-5. The overall characteristics of the composites containing 13X and ZSM-5 zeolites decreased as expected due to lower specific surface areas and micro- and mesopore volumes.

Concerning the Archimedes density measurements, the inclusion of various clays with ZSM-5 zeolite did not result in a notable variation in the densities of the biocarriers. The combination of 13X and bentonite exhibited the lowest density.

The findings of nanoindentation tests indicate that the biocarriers composed of 13X exhibit higher hardness and modulus of elasticity compared to those made of ZSM-5. It is noteworthy that the hardness and modulus of elasticity are generally within the same range, except for the ZSM-5/Halloysite Nanotubes combination, which has a significantly lower modulus of elasticity, one order of magnitude below the others, while the highest hardness value was attained with the 13X/Montmorillonite combination. The compression test results indicate that biocarriers made of 13X exhibit greater resistance to compression. The impact of inorganic binders does not exhibit a consistent pattern across all biocarriers. The combination of 13X and montmorillonite demonstrates the highest compressive strength. In addition, a computational model was employed to evaluate the stress response of 3D-printed specimens under compression. The mechanical test results suggest that combining computationally generated (FEA) compression test data with actual measurements

provides a dependable method to assess the mechanical deformation behavior of 3D-printed lattice biocarriers.

Author Contributions: "Conceptualization, T.S.; methodology, D.T., G.R., V.M. and P.F..; software, D.T.; validation, G.R., E.A.O. and V.M.; formal analysis, S.K. and K.T..; investigation, E.A.O.; resources, T.S.; data curation, S.K. and I.D.; writing—original draft preparation, E.A.O., G.T., I.D., K.T. and S.K., ; writing—review and editing, G.R., S.K., K.T.; visualization, S.K.; supervision, T.S., D.T. and G.R.; project administration, T.S.; funding acquisition, T.S.. All authors have read and agreed to the published version of the manuscript."

Funding: This research was co-funded by the European Regional Development Fund of the Eu- ropean Union and Greek national funds through the Operational Program Competitiveness, En- trepreneurship and Innovation, under the call RESEARCH—CREATE—INNOVATE (project code: T2EDK-00362).

Data Availability Statement: The data presented in this study are available upon request from the corresponding author.

Acknowledgments: The authors acknowledge all staff members of Qlab P.C. for their individual roles that contributed to the implementation of this study.

Conflicts of Interest: The authors declare that they have no known competing financial interests or personal relationships that could have appeared to influence the work reported in this paper.

References

1. Osman, A. I.; Hefny, M.; Abdel Maksoud, M. I. A.; Elgarahy, A. M.; Rooney, D. W. Recent Advances in Carbon Capture Storage and Utilisation Technologies: A Review. *Environmental Chemistry Letters*. Springer Science and Business Media Deutschland GmbH April 1, 2021, pp 797–849. https://doi.org/10.1007/s10311-020-01133-3.
2. Evgeniy G. Gordeev and Valentine P. Ananikov 2020 Russ. Chem. Rev. 89 1507 10.1070/RCR4980
3. A. Aranzabal, D. Iturbe, M. Romero-Sáez, M.P. González-Marcos, J.R. González-Velasco, J.a. González-Marcos, Optimization of process parameters on the extrusion of honeycomb shaped monolith of H-ZSM-5 zeolite, Chem. Eng. J. 162 (2010) 415–423, http://dx.doi.org/10.1016/j.cej.2010.05.043.
4. Y.-J. Lee, Y.-W. Kim, K.-W. Jun, N. Viswanadham, J.W. Bae, H.-S. Park, Textural properties and catalytic applications of ZSM-5 monolith foam for methanol conversion, Catal. Lett. 129 (2009) 408–415, http://dx.doi.org/10.1007/s10562-008-9811-z.
5. Y.-J. Lee, J.S. Lee, Y.S. Park, K.B. Yoon, Synthesis of large monolithic zeolite foamswith variable macropore architectures, Adv. Mater. 13 (2001) 1259, http://dx.doi.org/10.1002/1521-4095(200108)13:16b1259::AID-ADMA1259N3.0.CO;2-U.
6. H. Yang, Z. Liu, H. Gao, Z. Xie, Synthesis and catalytic performances of hierarchicalSAPO-34 monolith, J. Mater. Chem. 20 (2010) 3227, http://dx.doi.org/10.1039/b924736j.
7. J.a. Lewis, J.E. Smay, J. Stuecker, J. Cesarano, Direct ink writing of three-dimensional ceramic structures, J. Am. Ceram. Soc. 89 (2006) 3599–3609, http://dx.doi.org/10.1111/j.1551-2916.2006.01382.x.
8. H. Shao, D. Zhao, T. Lin, J. He, J.Wu, 3D gel-printing of zirconia ceramic parts, Ceram. Int. (2017) 3–7, http://dx.doi.org/10.1016/j.ceramint.2017.07.124.
9. J.-Y. Lee, J. An, C.K. Chua, Fundamentals and applications of 3D printing for novel materials, Appl. Mater. Today 7 (2017) 120–133, http://dx.doi.org/10.1016/j.apmt.2017.02.004.
10. D. Bourell, J.P. Kruth,M. Leu, G. Levy, D. Rosen, A.M. Beese, A. Clare, Materials for additive manufacturing, CIRP Ann. Manuf. Technol. (2017) http://dx.doi.org/10.1016/j.cirp.2017.05.009.
11. J. Zhu, Y. Fan, N. Xu, Journal of Membrane Science 367 (2011) 14.
12. Z. Shan, W. Van Kooten, Microporous and Mesoporous Materials 34 (2000) 81.
13. J.M. Zamaro, E.E. Miró, Chemical Engineering Journal 165 (2010) 701.
14. A. Aranzabal, D. Iturbe, M.P. González-Marcos, J.a. González-Marcos, J.R. González- Velasco, M. Romero-Sáez, EP2 412 672 A1, 2012.
15. Shao, Yun, et al. Emerging 3D printing strategies for enzyme immobilization: materials, methods, and applications. ACS omega 7.14 (2022): 11530-11543.
16. Montalvo, Silvio, et al. "Application of zeolites for biological treatment processes of solid wastes and wastewaters–A review." Bioresource Technology 301 (2020): 122808
17. Nikolaeva, S., et al. "Kinetics of anaerobic degradation of screened dairy manure by upflow fixed bed digesters: effect of natural zeolite addition." Journal of Environmental Science and Health Part A 44.2 (2009): 146-154.
18. Koltsakidis, S., Koidi, V., Lappas, A. et al. Influence of binder concentration in zeolitic ZSM-5/bentonite 3D-printed monoliths manufactured through robocasting for catalytic applications. Int J Adv Manuf Technol 126, 259–271 (2023). https://doi.org/10.1007/s00170-023-11091-z.

19. Lawson, Shane, et al. “Binderless zeolite monoliths production with sacrificial biopolymers.” Chemical Engineering Journal 407 (2021): 128011.
20. J. Lefevere, L. Protasova, S. Mullens, V. Meynen, 3D-printing of hierarchical porous ZSM-5: The importance of the binder system, Materials & Design, 134,331-341 (2017)https://doi.org/10.1016/j.matdes.2017.08.044.
21. Wang, Zongping, et al. “Removal of Microcystis aeruginosa by UV-activated persulfate: performance and characteristics.” Chemical Engineering Journal 300 (2016): 245-253.].
22. Kladovasilakis, N.; Charalampous, P.; Tsongas, K.; Kostavelis, I.; Tzetzis, D.; Tzovaras, D. Experimental and Computational Investigation of Lattice Sandwich Structures Constructed by Additive Manufacturing Technologies. J. Manuf. Mater. Process. 2021,5, 95.
23. Oliver, W.C., Pharr, G.M. An improved technique for determining hardness and elastic modulus using load and displacement sensing indentation experiments. Journal of Materials Research 7, 1564–1583 (1992). https://doi.org/10.1557/JMR.1992.1564.
24. G. Mansour, D. Tzetzis, D., K.D. Bouzakis, A Nanomechanical Approach on the Measurement of the Elastic Properties of Epoxy Reinforced Carbon Nanotube Nanocomposites, Tribology in Industry, Vol. 35 (3), pp.190-199, 2013.
25. K. Tsongas, D. Tzetzis, A. E. Karantzalis, G. Banias, D. Ahmadkhaniha, C. Zanella, T. E. Matikas, D. Bochtis, Microstructural, Surface Topology and Nanomechanical Characterization of Electrodeposited Ni-P/SiC Nanocomposite Coatings, Applied Sciences (Switzerland), Vol. 9 (14), 2901, 2019 https://doi.org/10.3390/app9142901.
26. Dong, Hai, et al. “Acidic hierarchical zeolite ZSM-5 supported Ru catalyst with high activity and selectivity in the seleno-functionalization of alkenes.” RSC advances 7.36 (2017): 22008-22016.
27. Chioti, Afroditi G., et al. "Characterization of Biofilm Microbiome Formation Developed on Novel 3D-Printed Zeolite Biocarriers during Aerobic and Anaerobic Digestion Processes." Fermentation 8.12 (2022): 746.